A discrete contact model for complex arbitrary-shaped convex geometries

Jan E. Marquardt [a, b, *], Ulrich J. Römer [c], Hermann Nirschl [b], Mathias J. Krause [a, b, d]

[a] Lattice Boltzmann Research Group, Karlsruhe Institute of Technology, Straße am Forum 8, Karlsruhe, 76131, Germany
[b] Institute for Mechanical Process Engineering and Mechanics, Karlsruhe Institute of Technology, Straße am Forum 8, Karlsruhe, 76131, Germany
[c] Institute of Engineering Mechanics, Karlsruhe Institute of Technology, Kaiserstraße 10, Karlsruhe, 76131, Germany
[d] Institute for Applied and Numerical Mathematics, Karlsruhe Institute of Technology, Englerstraße 2, Karlsruhe, 76131, Germany

ARTICLE INFO

Keywords:
Partially saturated cells method
Homogenized lattice Boltzmann method
Arbitrarily shaped particle
Discrete contact model
Particle-resolved simulation
OpenLB

ABSTRACT

The shape of particles has a significant influence on the behavior of suspensions, as the particle fluid, particle particle, and particle wall interactions depend on it. However, the simultaneous consideration of complex particle shapes and four way coupling remains a major challenge. This is mainly due to a lack of suitable contact models. Contact models for complex shapes have been proposed in literature, and most limit the accuracy of the particle fluid interaction. For this reason, this paper presents a novel contact model for complex convex particle shapes for use with partially saturated methods, in which we propose to obtain necessary contact properties, such as the indentation depth, by a discretization of the contact area. The goal of the proposed model is to enable comprehensive and accurate studies of par ticulate flows, especially with high volume fractions, that lead to new insights and contribute to the improvement of existing industrial processes. To ensure correctness and sustainability, we validate the model extensively by studying cases with and without fluid. In the latter case, we use the homogenized lattice Boltzmann method. The provided investigations show a great agreement of the proposed discrete contact model with analytical solutions and the literature.

1. Introduction

Particle laden flows are essential in many fields such as solid liquid separation and food processing. In various applications, a high particle concentration is present and, therefore, modeling requires four way coupling. Thus, besides coupling of the fluid to the particle (one way coupling) and particle to the fluid (two way coupling), particle particle and particle wall interactions are also essential for a correct investigation. In food processing, for instance, the accurate calculation of acting forces is indispensable to avoid damage to the particulate phase, as this would reduce the quality of the end product.

An option to consider individual particles is the use of the discrete element method (DEM), which has many applications (Zhu et al., 2008). Resolving an arbitrary geometry is, e.g., possible by a simple approach of glued spheres (Nolan & Kavanagh, 1995). Kodam et al. (2010) apply the same logic to model contacts of more complex shapes. In a similar fashion, the framework Grains3D (Rakotonirina & Wachs, 2018; Wachs et al., 2012) enables modeling the contact of non convex particle geometries through a descrip tion of glued convex shapes (Rakotonirina et al., 2019). Yet, the arbitrary shapes' approximation by, e.g., spheres leads to a limited accuracy. To increase the accuracy, the number of sphere segments must also increase immensely, leading to expensive computations. Additionally, to model the influence of a surrounding fluid remains a challenge as all the above mentioned models consider dry colli sions. Although, studies regarding the coupling with a surrounding fluid exist. However, these mostly use simple spherical geometries (Qiu & Wu, 2014; Sun & Xiao, 2016) or solely model the drag co efficient and lack a back coupling from the particles to the fluid (Weers et al., 2022). Thus, to process an accurate four way coupling with realistic and complex shapes, resolving these by direct nu merical simulations (DNS) is necessary.

Nagata et al. (2020) proposed an immersed boundary method (IBM) collision algorithm that is suitable for arbitrary shapes and

* Corresponding author. Lattice Boltzmann Research Group, Karlsruhe Institute of Technology, Straße am Forum 8, Karlsruhe, 76131, Germany.
E-mail address: jan.marquardt@kit.edu (J.E. Marquardt).

Nomenclature

Acronyms

BGK	Bhatnagar–Gross–Krook
DEM	discrete element method
DNS	direct numerical simulations
EDM	exact difference method
EOC	experimental order of convergence
HLBM	homogenized lattice Boltzmann method
IBM	immersed boundary method
LBM	lattice Boltzmann method
MEA	momentum exchange algorithm
PSM	partially saturated cells method
SDF	signed distance function

Roman Symbols

A_i	estimated corresponding surface of the ith surface cell
$\boldsymbol{C}$	point of impact
c	damping constant
$\boldsymbol{c}_i$	ith discrete lattice velocity
c_s	lattice speed of sound
D	dimension
d	indentation depth/displacement
d_B	HLBM model parameter
d_s	signed distance to a surface
$\dot{d}_{\mathrm{n}}$	relative velocity of two bodies in direction of the normal contact force
E	modulus of elasticity
E^*	effective modulus of elasticity
E_{A}	modulus of elasticity of an object A
E_{B}	modulus of elasticity of an object B
e	signed coefficient of restitution
$\boldsymbol{F}_{\mathrm{f}}$	external forces acting on the fluid
$\boldsymbol{F}_{\mathrm{n}}$	normal contact force
F_{n}	magnitude of the normal contact force
$\boldsymbol{F}_{\mathrm{p}}$	forces acting on a particle
$\boldsymbol{F}_{\mathrm{p,h}}$	hydrodynamic forces acting on a particle
$\boldsymbol{F}_{\mathrm{t}}$	tangential contact force
F_{t}	magnitude of the tangential contact force
f_i	ith particle distribution function
$f_i\mathrm{eq}$	ith equilibrium distribution
f_i^*	ith post collision distribution
H	cylinder height
I	the sphere's moment of inertia
$\boldsymbol{I}_{\mathrm{p}}$	particle's moment of inertia
I_{xx}	moment of inertia with respect to x axis
I_{yy}	moment of inertia with respect to y axis
I_{zz}	moment of inertia with respect to z axis
k	parameter for calculation of normal contact force
m	particle mass
N	resolution of a characteristic length for the LBM simulation
N_{c}	resolution of the overlap of the particles in contact
$\boldsymbol{n}_{\mathrm{c}}$	contact normal
n_{cell}	number of cells in the overlap
$n_{\mathrm{cell,s}}$	number of cells on the surface of the overlap
$\boldsymbol{n}_{\mathrm{s},i}$	surface normal of the ith surface grid point
n_{t}	number of sub time steps
p	pressure
R	radius
R_{i}	radius of object i
R_{r}	reduced radius
r	distance between the cylinder's center and the contact point
S_i	source term
$\boldsymbol{T}_{\mathrm{p}}$	torque acting on a particle
$\boldsymbol{T}_{\mathrm{p,h}}$	torque acting on a particle caused by hydrodynamic forces
t	time
$\boldsymbol{u}$	fluid velocity
V_{c}	overlap volume
V_{cell}	volume of a single cell
$\boldsymbol{v}$	particle velocity
$\boldsymbol{v}_{\mathrm{A}}$	velocity of a rigid body A
$\boldsymbol{v}_{\mathrm{AB}}$	relative velocity of two objects (A and B)
$\boldsymbol{v}_{\mathrm{AB,n}}$	relative normal velocity of two objects (A and B)
$\boldsymbol{v}_{\mathrm{AB,t}}$	relative tangential velocity of two objects (A and B)
$\boldsymbol{v}_{\mathrm{B}}$	velocity of a rigid body B
$\boldsymbol{v}_{\mathrm{p}}$	velocity at the particle's center of mass
v_s	velocity at which the transition from static to kinetic friction takes place
$v_{\mathrm{z}+}$	rebound velocity in z direction
v_{z}	initial velocity in z direction
w_i	ith weight for the equilibrium distribution calculation
$\boldsymbol{X}_i$	centroid of the ith cell in the overlap
$\boldsymbol{x}$	position in the global coordinate system of the simulation
$\widetilde{\boldsymbol{x}}$	position in the local coordinate system located at the particle's center of mass
$\boldsymbol{x}_{\mathrm{c}}$	contact point
$\boldsymbol{x}_m$	the particle's center of mass in the global coordinate system of the simulation
$\boldsymbol{x}_{\mathrm{max}}$	maximum coordinate of the contact enclosing cuboid (bounding box)
$x_{\mathrm{max},j}$	jth component of the bounding boxes maximum coordinate
$\boldsymbol{x}_{\mathrm{min}}$	minimum coordinate of the contact enclosing cuboid (bounding box)
$x_{\mathrm{min},j}$	jth component of the bounding boxes minimum coordinate

Greek Symbols

α	angle between the line from the contact point to the cylinder center and the face of the cylinder
Δt	time step size
Δt_{c}	differing time step size for solution of equations of motion with existing contact
$\Delta\boldsymbol{u}$	difference between fluid and particle velocity
Δx	spacing between two neighboring lattice cells
$\Delta x_{c,j}$	spacing between two neighboring points on the overlap grid in the j direction
η	dynamic viscosity
θ	impact angle
μ_{k}	coefficient for kinetic/sliding friction
μ_{s}	coefficient for static friction
ν	Poisson's ratio
ν_{A}	Poisson's ratio of an object A
ν_{B}	Poisson's ratio of an object B
ρ	fluid density
τ	relaxation time
Ω_i	collision operator
$\boldsymbol{\omega}$	angular velocity
$\omega_{\mathrm{y}+}$	rebound angular velocity about the y axis

shows good accuracy for simple geometries. The underlying IBM resolves surfaces using Lagrange points (Uhlmann, 2005). These points interact with the fluid, but need not depend on the particular fluid grid. As a result, IBM achieves a high accuracy. However, the frequent interpolations between particle and fluid points are costly. Also, it is beneficial that it is coupleable with different approaches for solving the fluid, such as the finite element method, the finite volume method, and the lattice Boltzmann method (LBM).

The latter, LBM, is of increasing interest as it is efficient and is easy to parallelize because costly computations are purely local (Succi, 2001). Other LBM based approaches to simulate arbitrary particle shapes also exist. The partially saturated cells method (PSM) is the most common and was first proposed by Noble and Torczynski (1998) in its original form. Since then, there have been several new approaches, such as the homogenized lattice Boltz mann method (HLBM) introduced by Krause et al. (2017). All PSMs use a level set function to describe an approximation of the volume fraction of the particle over the complete computation domain (Haussmann et al., 2020). Previous studies using HLBM show that it allows representation of almost every shape (Trunk et al., 2018, 2021a, 2021b). Since the method uses the LBM voxel representa tion, the approximation of the shape, depends on the grid, and very thin objects are prone to problems. Though PSMs have shown po tential, modeling the contact of arbitrary shaped particles, which is essential to consider realistic suspensions with high particle con centrations, remains a big challenge. Although previous studies show that lubrication forces suffice to decelerate particles, the in fluence of contacts is still incorrectly represented (Trunk et al., 2021a).

The aim of this paper is to provide a model to consider the contact of complex convex particle shapes to close the above gap. The literature lacks viable options to consider high particle volume fractions along with fluid interaction, when the particle geometry is realistic and complex. For this purpose, we propose a discretized contact model that is useable along with PSMs, such as HLBM. In other words, this paper introduces a novel model for dense sus pensions using PSMs and validates it on suitable test cases. The associated simulations for validation use OpenLB (Krause et al., 2020a, 2020b).

To introduce the method and its applicability, the paper adopts the following structure. In Section 2, the models used to consider the fluid, particles, and interactions are introduced. In Section 3, we discuss the numerical methods that are used to solve the model system. This is followed by a validation of the novel method for contact treatment and its application in a system with and without a particle laden viscous fluid in Sections 4 and 5. Finally, in Section 6, we give a summary and draw a conclusion.

2. Modeling

Suspensions consist of fluids and particles. Both components need to be described by a proper model. This also applies to the particle particle and particle wall interaction in the presence of a high particle concentration. For these interactions, the geometries of the objects under consideration are of great importance. Therefore, we show the models for fluids in Section 2.1, for particles in Section 2.2, for geometries in Section 2.3, and for contacts in Section 2.4.

2.1. Fluid

We describe the fluid component by the incompressible Navier–Stokes equations:

$$\begin{aligned} \frac{\partial \boldsymbol{u}}{\partial t} + (\boldsymbol{u}\cdot\nabla)\boldsymbol{u} \quad \frac{\eta}{\rho}\Delta\boldsymbol{u} + \frac{1}{\rho}\nabla p \quad & \boldsymbol{F}_{\mathrm{f}}, \\ \nabla\cdot\boldsymbol{u} \quad & 0, \end{aligned} \tag{1}$$

where $\boldsymbol{u}$ is the fluid velocity, t the time, p the pressure, $\boldsymbol{F}_{\mathrm{f}}$ the total of all forces acting on the fluid, e.g., gravity, η and ρ are the fluid's dynamic viscosity and density.

2.2. Particle

To consider particles, we need to describe the particle motion and represent the particle's shape. For the former, we use Newton's second law of motion. The translation is then given by

$$m\frac{\partial \boldsymbol{v}_{\mathrm{p}}}{\partial t} \quad \boldsymbol{F}_{\mathrm{p}} \tag{2}$$

and the rotational motion by

$$\boldsymbol{I}_{\mathrm{p}}\frac{\partial \omega}{\partial t} \quad \boldsymbol{T}_{\mathrm{p}}. \tag{3}$$

In the above mentioned equations, m, $\boldsymbol{I}_{\mathrm{p}}$, $\boldsymbol{v}_{\mathrm{p}}$, ω, $\boldsymbol{F}_{\mathrm{p}}$, $\boldsymbol{T}_{\mathrm{p}}$ are the par ticle's mass, moment of inertia, velocity, angular velocity, and the sum of forces as well as torque acting on the particle. Here, all quantities with index p refer to the particle's center of mass. Note that in this work $\boldsymbol{F}_{\mathrm{p}}$ is composed of hydrodynamic forces $\boldsymbol{F}_{\mathrm{p,h}}$, normal and tangential contact forces $\boldsymbol{F}_{\mathrm{n}}$ and $\boldsymbol{F}_{\mathrm{t}}$. The torque acting on the particle $\boldsymbol{T}_{\mathrm{p}}$ also stems from the hydrodynamic and the contact forces. For the latter, the lever results from the difference between the contact point $\boldsymbol{x}_{\mathrm{c}}$ and the center of mass of the particle $\boldsymbol{x}_{\mathrm{m}}$.

2.3. Geometries

In this work, we use signed distance functions (SDFs) to describe the geometries of the particles and walls. Since a comprehensive discussion of these would exceed the scope of this paper, the interested reader is referred to the literature (Hart, 1996; Haugo et al., 2017) for more information.

We use SDFs to determine the signed distance d_{s} of a point $\boldsymbol{x}$ to a surface $B \in \mathbb{R}^D$ with the dimension D. Here, the sign indicates whether the point $\boldsymbol{x}$ is inside or outside the geometry. This distance to the surface is particularly valuable for contact modeling and al lows us to derive a significant part of the necessary quantities. For example, the normal on the geometry surface is obtained from the derivative of the SDF. Stemming from computer graphics, SDFs are also highly efficient. These advantages make them a perfect fit for the application discussed here.

Henceforth, we use

$$d_{\mathrm{s}}(\tilde{\boldsymbol{x}}) \quad \|\tilde{\boldsymbol{x}}\| \quad R \tag{4}$$

to describe spheres and

$$d_{\mathrm{s}}(\tilde{\boldsymbol{x}}) \quad \max\left(\left\|(\tilde{x}_x, \tilde{x}_y)\right\| \quad R, \tilde{x}_z \quad H/2\right) \tag{5}$$

to represent cylinders which have an axis orthogonal to the x y plane. Here, R is the radius, H the cylinder's length and $\boldsymbol{x}$ is location relative to the center of mass of the respective geometry. The transformation from the global coordinate system of the simulation into the coordinate system of the geometry uses translation and rotation depending on the motion of the particle.

2.4. Contact

In order to describe interactions of arbitrary geometries, we use a model proposed by Nassauer and Kuna (2013) to compute the normal, Section 2.4.1, and tangential, Section 2.4.2, contact force from an overlap volume. The commonly very small overlap models deformation during the contact and does not occur in reality.

2.4.1. Normal contact

Following this model, the normal contact force's magnitude reads

$$F_{\mathrm{n}} \quad E^{*} k \sqrt{V_{\mathrm{c}} d}\left(1 + c\dot{d}_{\mathrm{n}}\right), \tag{6}$$

with the effective modulus of elasticity E^*, a constant k, the overlap volume V_{c}, the indentation depth d, a damping constant c, and the magnitude of the relative velocity between two bodies in contact in the direction of the normal force $\dot{d}_{\mathrm{n}}$. The former is given as

$$E^{*} \quad \left.\frac{1 \quad \nu_{\mathrm{A}}^{2}}{E_{\mathrm{A}}} + \frac{1 \quad \nu_{\mathrm{B}}^{2}}{E_{\mathrm{B}}}\right)^{-1}. \tag{7}$$

Here, E_{A} and ν_{A} are the modulus of elasticity and the Poisson's ratio of objects A and E_{B} and ν_{B} of object B, which are in contact.

The constant $k \quad 4/(3\sqrt{\pi})$ applies to a sphere–half space and sphere–sphere contact (Nassauer & Kuna, 2013). For a cylindrical flat punch, on the other hand, $k \quad 2/\sqrt{\pi}$ applies.

By multiplication with the contact normal $\boldsymbol{n}_{\mathrm{c}}$, we obtain vector components from the magnitude of the force

$$\boldsymbol{F}_{\mathrm{n}} \quad \boldsymbol{n}_{\mathrm{c}} F_{\mathrm{n}}, \tag{8}$$

which is necessary for solving the particle motion equations, see Eqs. (2) and (3).

To solve the above mentioned model equations, we need to determine the overlap volume V, indentation depth d, and contact normal $\boldsymbol{n}_{\mathrm{c}}$ numerically, as presented in Section 3.3.

Also, a correct damping factor, which depends on the initial relative velocity in the normal contact direction, is crucial. How ever, the consideration of this correlation is beyond the scope of this paper. Nevertheless, it is vital to evaluate the applicability of existing models from the literature (Alves et al., 2015; Carvalho & Martins, 2019) in future works.

2.4.2. Tangential contact

Tangential forces occur due to friction. Commonly, friction de pends on the normal force, see Eq. (6), and the coefficients of static and kinetic/sliding friction, μ_{s} and μ_{k}, respectively. Nassauer and Kuna (2013) follow a similar logic and describe the magnitude of the friction force by

$$F_{\mathrm{t}} \quad \left(\left(2\mu_{\mathrm{s}}^{*} \quad \mu_{\mathrm{k}}\right)\frac{a^{2}}{a^{4}+1} + \mu_{\mathrm{k}} \quad \frac{\mu_{\mathrm{k}}}{a^{2}+1}\right)F_{\mathrm{n}}, \tag{9}$$

with

$$\mu_{\mathrm{s}}^{*} \quad \mu_{\mathrm{s}} \quad \left. 1 \quad 0.09\left(\frac{\mu_{\mathrm{k}}}{\mu_{\mathrm{s}}}\right)^{4}\right), \tag{10}$$

and

$$a \quad \frac{\left\|\boldsymbol{v}_{\mathrm{AB,t}}(\boldsymbol{x}_{\mathrm{c}})\right\|}{v_{s}}. \tag{11}$$

Here, we use the relative tangential velocity $\boldsymbol{v}_{\mathrm{AB,t}}$ at the contact point $\boldsymbol{x}_{\mathrm{c}}$ of the objects A and B that are in contact and the model parameter v_s, which denotes the velocity at which a transition from static to kinetic friction occurs. The friction force acts against the relative tangential velocity $\boldsymbol{v}_{\mathrm{AB,t}}$ and thus

$$\boldsymbol{F}_{\mathrm{t}} \quad F_{\mathrm{t}} \frac{\boldsymbol{v}_{\mathrm{AB,t}}(\boldsymbol{x}_{\mathrm{c}})}{\left\|\boldsymbol{v}_{\mathrm{AB,t}}(\boldsymbol{x}_{\mathrm{c}})\right\|} \tag{12}$$

applies.

3. Numerical methods

3.1. Lattice Boltzmann method

To solve the incompressible Navier–Stokes equations mentioned in Section 2.1, we use the lattice Boltzmann method (LBM) (Krüger et al., 2017; Succi, 2001; Sukop & Thorne, 2006).

The origin of LBM is gas kinetics, and for this reason, it operates on a mesoscopic scale and considers particle populations. We describe these populations by a discrete velocity distribution function $f_i(\boldsymbol{x}, t)$. The arguments of the particle populations, the position $\boldsymbol{x}$ and the time t, are discrete. Also, there is a discrete set of velocities $\boldsymbol{c}_i$, which is predetermined. For example, in the following, we use a D3Q19 velocity set for all of our simulations, which operates in a three dimensional space and has 19 discrete velocities (Krüger et al., 2017; Succi, 2001). We can additionally use the dis tribution function to calculate macroscopic quantities, such as density $\rho(\boldsymbol{x}, t) \quad \sum_i f_i(\boldsymbol{x}, t)$ and velocity $\rho\boldsymbol{u}(\boldsymbol{x}, t) \quad \sum_i \boldsymbol{c}_i f_i(\boldsymbol{x}, t)$.

To compute the distribution function's value in the next time step, we use the lattice Boltzmann equation (LBE) with an addi tional source term $S_i(\boldsymbol{x}, t)$ to account for forces acting on the fluid $\boldsymbol{F}_{\mathrm{f}}$, which in this context is the influence of submerged particles via the HLBM, see Section 3.2. The LBE is usually utilized with a time step size $\Delta t \quad 1$ in lattice units and divided into two distinct parts. The collision step

$$f_i^{*}(\boldsymbol{x}, t) \quad f_i(\boldsymbol{x}, t) + \Omega_i(\boldsymbol{x}, t) + S_i(\boldsymbol{x}, t), \tag{13}$$

with the collision operator Ω_i, through which we obtain the post collision distributions f_i^*, and the streaming step

$$f_i(\boldsymbol{x} + \boldsymbol{c}_i, t+1) \quad f_i^{*}(\boldsymbol{x}, t), \tag{14}$$

which distributes the post collision distribution f_i^* to the neigh boring lattice nodes. Furthermore, we use the Bhatnagar–Gross–Krook (BGK) collision operator (Bhatnagar et al., 1954), which is given by

$$\Omega_i(\boldsymbol{x}, t) \quad \frac{f_i(\boldsymbol{x}, t) \quad f_i^{\mathrm{eq}}(\rho, \boldsymbol{u})}{\tau}, \tag{15}$$

where τ is the relaxation time that governs the speed of the particle populations' relaxation towards its equilibrium state. The equilib rium is given by the discrete Maxwell–Boltzmann distribution

$$f_i^{\mathrm{eq}}(\rho, \boldsymbol{u}) \quad w_i \rho \quad \left. 1 + \frac{\boldsymbol{c}_i \cdot \boldsymbol{u}}{c_s^2} + \frac{(\boldsymbol{c}_i \cdot \boldsymbol{u})^2}{2c_s^4} + \frac{\boldsymbol{u}^2}{2c_s^2}\right). \tag{16}$$

The necessary weights w_i and constant lattice speed of sound c_s depend on the chosen velocity set. The former comes from a Gauss–Hermite quadrature rule, and $c_s \quad 1/\sqrt{3}$ when using a D3Q19 set.

3.2. Homogenized lattice Boltzmann method

Trunk et al. (2021a) distinguish between three different elements in the method. Namely, object representation, forcing scheme, and momentum exchange.

The former uses a voxel representation, which was explained in detail by Trunk et al. (2018). This representation allows to calculate necessary physical properties such as volume, mass, center of mass, and moment of inertia. Additionally, we map the particle onto the fluid domain during this step. For this, we use a model parameter $d_B \in [0, 1]$ to calculate the local velocity difference

$$\Delta \boldsymbol{u}(\boldsymbol{x}, t) \quad d_B(\boldsymbol{x}, t)(\boldsymbol{v}(\boldsymbol{x}, t) \quad \boldsymbol{u}(\boldsymbol{x}, t)). \tag{17}$$

Here, $\boldsymbol{v}(\boldsymbol{x}) \quad \boldsymbol{v}(\boldsymbol{x}_m) + \omega \times (\boldsymbol{x} \quad \boldsymbol{x}_m)$ is the particle's velocity at position $\boldsymbol{x}$, and $\boldsymbol{x}_m$ is the particle's center of mass. The aforementioned smoothing at the particle surface uses trigonometric functions, as described by Krause et al. (2017), with the signed distance to the particle surface. We use

$$d_B(\boldsymbol{x}, t) \quad x \quad \begin{cases} 1 & \text{if } d_s \leq \quad \epsilon/2 \\ \cos^2\left(\pi\left(\frac{d_s}{\epsilon} + \frac{1}{2}\right)\right) & \text{if } \epsilon/2 > d_s > \quad \epsilon/2 \\ 0 & \text{if } d_s \geq \epsilon/2 \end{cases} \tag{18}$$

to compute the model parameter and set the size of the smooth boundary via the parameter ϵ.

Since studies by Trunk et al. (2021a) show that it provides the best results, we use the adaption of the exact difference method (EDM) by Kupershtokh et al. (2009) as the forcing scheme as well. The method solely uses the source term

$$S_i(\boldsymbol{x}, t) \quad f_i^{\mathrm{eq}}(\rho, \boldsymbol{u} + \Delta \boldsymbol{u}) \quad f_i^{\mathrm{eq}}(\rho, \boldsymbol{u}) \tag{19}$$

in Eq. (13) with the above mentioned local velocity difference $\Delta \boldsymbol{u}$, see Eq. (17).

To obtain the hydrodynamic force acting on the particle $\boldsymbol{F}_{\mathrm{p,h}}$ and the resulting torque $\boldsymbol{T}_{\mathrm{p,h}}$, we use the momentum exchange algorithm (MEA) by Wen et al. (2014). We then compute the acceleration from the resulting hydrodynamic force along with other forces, such as gravitation and buoyancy, via Newton's second law of motion and use it within an explicit time integration scheme. Here, we choose the velocity Verlet algorithm (Swope et al., 1982; Verlet, 1967) to solve the equations of motion.

3.3. Discrete contacts

In the following, we propose a discrete method to treat particle particle and particle wall interactions. To do so, we need to find a simple cuboid with which the contact geometry is enclosed, see Section 3.3.1. In the following, we refer to this enclosing cuboid as bounding box. Afterwards, we must correct this bounding box as presented in Section 3.3.2. We then iterate over the improved bounding box with discrete steps to calculate the contact properties in Section 3.3.3. The necessary steps and their outcome are illustrated in Fig. 1.

3.3.1. Contact detection

In Fig. 1(a), we see an exemplary contact. For simplification, this is a 2D contact, however, the following analogously applies to 3D. It is easy to see that the two objects are in contact. However, this is much more difficult to determine numerically for complex geometries.

To overcome this challenge, we use a very simple detection while setting the HLBM model parameter d_B on the lattice, since in both cases, we have a dependency on the signed distance d_s. For clarity, Fig. 1(b) shows the magnified contact area with the lattice drawn in gray. Each grid point where the signed distance to both object surfaces is less than half of a cell's diagonal, $d_s < 0.5\sqrt{D}\Delta x$, with the considered dimension D, we consider being inside the overlap. If a point is inside the contact according to the previously mentioned condition, we update the minimum and maximum coordinates, $\boldsymbol{x}_{\min}$ and $\boldsymbol{x}_{\max}$, of the bounding box, represented by the dashed line. Because of this, Fig. 1(b) illustrates an overestimation of the bounding box. This is advantageous, however, as it increases the accuracy and stability. Otherwise, a higher fraction of the overlap is incorrect and, for the next step presented in Section 3.3.2, an overestimation is better than an underestimation. Because underestimation can lead to erroneous missing contact detections that are impossible to correct with currently known approaches and reasonable effort.

The contacts found are saved in contact objects. For example, we store the particle IDs and the minimum as well as maximum coordinates, $\boldsymbol{x}_{\min}$ and $\boldsymbol{x}_{\max}$, of the bounding box of the contact for particle particle contacts in it. For particle wall interactions, we solely need to replace one particle ID with an identifier for the wall. This means that all data is available for the later correction of the bounding box (Section 3.3.2) or contact force calculation (Section 3.3.3).

The aforementioned identifiers are, e.g., simple indices of a field which stores the particles or walls. Naturally, other implementations are also plausible. It is only important that this identifier is unique and constant during the contact treatment, or, if a change is absolutely necessary, then the changes must also be applied to the contact object.

3.3.2. Correct detected contacts

Since the rough contact detection most likely overestimates the bounding box, we need to shrink it to the actual contact, using Algorithm 1. This step causes the change from Fig. 1(b) to (c). Thereby, we improve the accuracy of the contact force calculation, which we discuss in Section 3.3.3. To do this, we first calculate a step size

$$\Delta x_{c,j} \quad \frac{1}{N_c} \begin{cases} \Delta x & \text{if } x_{\max,j} \quad x_{\min,j} \quad 0, \\ (x_{\max,j} \quad x_{\min,j}) & \text{if } x_{\max,j} \quad x_{\min,j} > 0. \end{cases} \tag{20}$$

with which we iterate over the overlap volume's bounding box per spatial direction j. This resolves the overlapping area with N_c cuboids, which may have different aspect ratios.

In the following, we iterate over the bounding box's surface, using the step sizes from Eq. (20). During this iteration, we determine the distances to the real contact surface, which is inside the bounding box, in different discrete directions. These directions change in 45° steps as illustrated for selected grid points (black disks) in Fig. 1(b). Based on the point on the surface, the direction and the distance determined, we can now identify points on the contact surface and derive an improved bounding box. The distance to the contact surface can be calculated, e.g., via ray marching or ray tracing.

In the end, we thus obtain a bounding box of the overlapping region of two identifiable objects. This gives us sufficient information to calculate the contact forces in the next step.

Algorithm 1. Algorithm to correct the initial bounding box.

```
Calculate step size for rough bounding box ;            ▷ See Eq. (20)
for all discrete positions inside the bounding box do
  if position is on bounding box surface then
    // Iterate over all discrete directions as
       illustrated in Fig. 1(b)
    for all discrete directions in 45° steps do
      if neighbor is inside the bounding box then
        // Calculate distance via ray marching or ray
           tracing
        Calculate distance to the collision surface;
        Determine position on the collision surface;
        Update the minimal and maximal bounding box
         coordinates;
      end
    end
  end
  collision & streaming;
end
```

3.3.3. *Calculation of contact forces*

Having obtained the bounding box, we continue with the calculation of the forces acting on the objects in contact. For this, we apply another uniform rectangular grid on the bounding box, as shown in Fig. 1(c), to obtain the necessary parameters for the calculation of the contact force. Some of them are shown in Fig. 1(d). We again compute the distance between the respective grid points from Eq. (20). To derive the contact information, as mentioned in Section 2.4, we evaluate if it lies within the contact (solid lines) or outside the contact (dashed lines), on each grid point, and count the total number of cells n_{cell} within the overlap.

Overlap volume. We then calculate the overlap volume V_{c} of two colliding objects by a sum of the volume of all individual cells that are within the contact:

$$V_{\mathrm{c}} = n_{\mathrm{cell}} V_{\mathrm{cell}}. \tag{21}$$

Here, V_{cell} is each cell's volume. In Fig. 1(c), we see that a point may lie right on the surface of the contact, which therefore would lead to an overestimation of the overlap volume. However, this is solely a discretization error and decreases drastically with an increased resolution. Also, in actual simulations, such an ideal contact is almost impossible, so, if at all, the minimum and maximum are on the surface of the contact and all other grid points are inside. It is therefore advantageous to use intersections of the grid lines and not the centers as it compensates for the otherwise missing volume to an extent.

Contact normal. Another required quantity is the contact normal $\boldsymbol{n}_{\mathrm{c}}$. We calculate it from the cells on the surface, but we use the first layer of grid points outside the contact. In Fig. 1(c), some considered points and their respective normals $\boldsymbol{n}_{\mathrm{s},i}$ are presented in blue. This leads to greater accuracy, because we have more cells in this layer than in the inner one for convex shapes. Additionally, we verify that a point is actually on the surface by checking that the neighbor in the direction of the normalized normal at the cell's center $\boldsymbol{n}_{\mathrm{s},i}$ is inside the overlap. The normal $\boldsymbol{n}_{\mathrm{s},i} = \nabla d_{\mathrm{s}}(\boldsymbol{x})$ is obtained from the derivative of the SDF at the corresponding position. To calculate this, we use the central difference method. Analogous to the procedure of Nassauer and Kuna (2013), we calculate the normal from a weighted average of the normals of the previously defined surface cells

$$\boldsymbol{n}_{\mathrm{c}} = \frac{\sum_i^{n_{\mathrm{cell,s}}} A_i \frac{\boldsymbol{n}_{\mathrm{s},i}}{\|\boldsymbol{n}_{\mathrm{s},i}\|}}{\sum_i^{n_{\mathrm{cell,s}}} A_i}. \tag{22}$$

Here, we sum over all surface cells $n_{\mathrm{cell,s}}$ and weigh each with the surface A_i, which is the cross section in the cell's normal direction $\boldsymbol{n}_{\mathrm{s},i}$. It is further important to note that we use $\boldsymbol{n}_{\mathrm{s},i} = -\nabla d_{\mathrm{s}}(\boldsymbol{x})$ for the second object in contact, so that the normals of both objects point in the same direction. We estimate A_i in 3D with

$$A_i = \begin{pmatrix} \Delta x_{c,y}\Delta x_{c,z} \\ \Delta x_{c,x}\Delta x_{c,z} \\ \Delta x_{c,x}\Delta x_{c,y} \end{pmatrix} \cdot \left(\frac{\boldsymbol{n}_{\mathrm{s},i}}{\|\boldsymbol{n}_{\mathrm{s},i}\|} \odot \frac{\boldsymbol{n}_{\mathrm{s},i}}{\|\boldsymbol{n}_{\mathrm{s},i}\|} \right), \tag{23}$$

and in 2D with

$$A_i = \begin{pmatrix} \Delta x_{c,y} \\ \Delta x_{c,x} \end{pmatrix} \cdot \left(\frac{\boldsymbol{n}_{\mathrm{s},i}}{\|\boldsymbol{n}_{\mathrm{s},i}\|} \odot \frac{\boldsymbol{n}_{\mathrm{s},i}}{\|\boldsymbol{n}_{\mathrm{s},i}\|} \right), \tag{24}$$

In the equations above, $\odot$ refers to the Hadamard product, i. e., an element-wise product.

Contact point. According to Nassauer and Kuna (2013), the contact point $\boldsymbol{x}_c$ is defined as the center of mass of the overlap volume. This can be determined by dividing this area into cuboids, as shown in Fig. 1(c), and by assuming that the particles have a constant density distribution. Then, we simply calculate the mean value of all cell centroids $\boldsymbol{X}_i$

$$\boldsymbol{x}_c = \frac{\sum_i^{n_{\mathrm{cell}}} \boldsymbol{X}_i}{n_{\mathrm{cell}}}. \tag{25}$$

Displacement. Now, the displacement d is to be determined. For this purpose, the distance from the contact point $\boldsymbol{x}_c$ to the contact surface is determined in two directions. On the one hand, in the direction of the contact's normal $\boldsymbol{n}_{\mathrm{c}}$ and, on the other hand, in the opposite direction $-\boldsymbol{n}_{\mathrm{c}}$. Both distances together result in the wanted displacement d, as illustrated in Fig. 1(d). The temporal change of the displacement d reads (Nassauer & Kuna, 2013)

$$\dot{d}_{\mathrm{n}} = \|\boldsymbol{v}_{\mathrm{AB,n}}(\boldsymbol{x}_c)\|. \tag{26}$$

Here, we use the relative velocity in normal direction (Džiugys & Peters, 2001)

$$\boldsymbol{v}_{\mathrm{AB,n}}(\boldsymbol{x}_c) = \left(\boldsymbol{v}_{\mathrm{AB}}(\boldsymbol{x}_c) \cdot \frac{\boldsymbol{n}_{\mathrm{c}}}{\|\boldsymbol{n}_{\mathrm{c}}\|} \right) \frac{\boldsymbol{n}_{\mathrm{c}}}{\|\boldsymbol{n}_{\mathrm{c}}\|}, \tag{27}$$

at the contact point $\boldsymbol{x}_c$. The total relative velocity of two objects in contact, A and B, is calculated via

$$\boldsymbol{v}_{\mathrm{AB}}(\boldsymbol{x}_c) = \boldsymbol{v}_{\mathrm{A}}(\boldsymbol{x}_c) - \boldsymbol{v}_{\mathrm{B}}(\boldsymbol{x}_c). \tag{28}$$

Tangential velocity. The tangential velocity is the difference between the total relative velocity $\boldsymbol{v}_{\mathrm{AB}}$ and its normal component $\boldsymbol{v}_{\mathrm{AB,n}}$ (Džiugys & Peters, 2001):

$$\boldsymbol{v}_{\mathrm{AB,t}} = \boldsymbol{v}_{\mathrm{AB}} - \boldsymbol{v}_{\mathrm{AB,n}}. \tag{29}$$

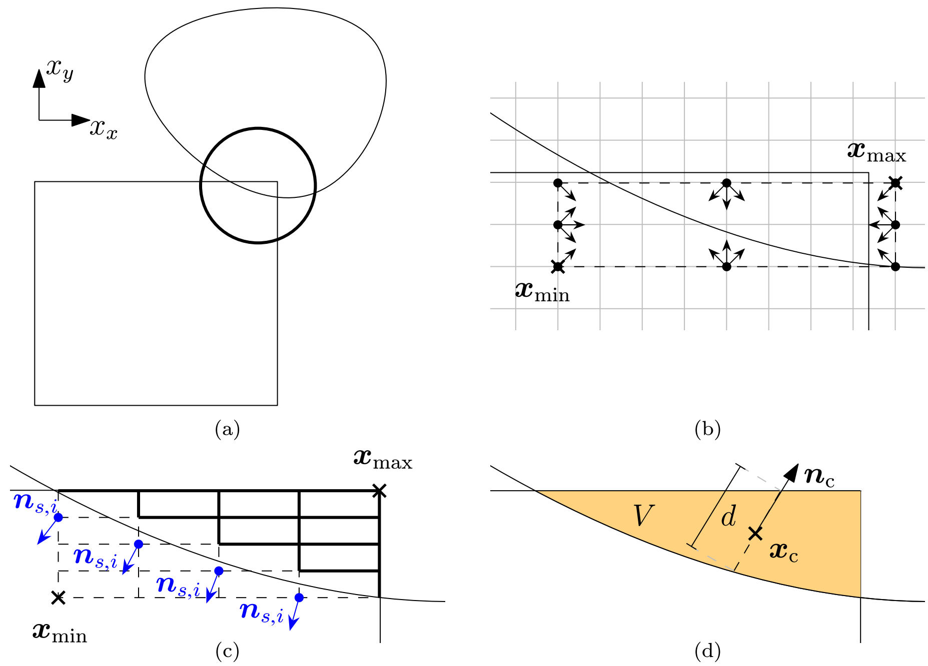

Fig. 1. Illustration of two convex objects in contact. Showing a rectangle and a rounded geometry and highlighting the overlap area with a thickened circle (a). (b) shows the magnified contact area with an example lattice in gray and the approximated bounding box. It also presents the magnified contact with the improved bounding box and the grid used for the calculation of all contact-relevant properties (c). Furthermore, the contact and the necessary properties are displayed in (d).

3.4. Time step algorithm with four way coupling

For a better overview, Algorithm 2 shows the basic LBM time step algorithm with the four way coupling. Here, the previously explained methods are listed in the necessary order. Additionally, we show the possibility of sub time steps solely for the solution of the equations of motion, with a time step size $\Delta t_{\mathrm{c}} \quad \Delta t/n_{\mathrm{t}}$, for $n_{\mathrm{t}} \in \mathbb{N}_{>0}$. Here, n_{t} is the number of sub time steps to process.

Algorithm 2. Basic LBM time step algorithm with four way coupling.

```
for all time steps do
    Couple f uid to particles;                          ▷ Using the MEA
    Couple particles to f uid with simultaneous, rough contact
     detection;                    ▷ Using the EDM and Section 3.3.1
    Communicate detected collisions;
    for all sub time steps do
        Correct bounding box;                      ▷ See Section 3.3.2
        Determine contact properties;              ▷ See Section 3.3.3
        Calculate contact force;                     ▷ See Section 2.4
        Add external forces;                           ▷ E.g.  gravity
        Solve equations of motion;
    end
    Delete empty collision objects;
    Perform collision and streaming;
    Increase time step;
end
```

4. Validation

In the subsequent section, we consider several cases for vali dation. First, in Section 4.1, we validate the normal contact force. This is followed by a cylinder wall impact test to check the resulting particle motion in Section 4.2.

4.1. Contact force

As a first challenge for the proposed method, we consider several contact problems with known analytical solutions, as described in Section 4.1.1. This is followed by the numerical results and a comparison of these with the analytical solutions in Section 4.1.2. Finally, in Section 4.1.3, we perform a grid independence study.

4.1.1. Setup

To validate the correctness of the normal contact force, we consider multiple test cases as illustrated in Fig. 2. The tests include: a contact between a sphere with radius R and a half space, see Fig. 2(a), a contact between two spheres with different radii R_1 and R_2, see Fig. 2(b), a cylindrical flat punch, see Fig. 2(c), and a contact between two perpendicular crossed cylinders with an equal radius R, see Fig. 2(d).

In the aforementioned tests, we increase the indentation depth incrementally and compare the results with given analytical solu tions. For a contact between a sphere with radius R and a half space, we expect the normal force (Popov et al., 2019)

$$F_{\mathrm{n}} \quad \frac{4}{3} E^{*} R^{1/2} d^{3/2}. \tag{30}$$

The equation looks similar for a contact between two crossed cyl inders with the same radius R and for a contact of two spheres with radii R_1 and R_2. However, for the latter we must replace the radius R with the effective radius R_{r} reading (Popov, 2017)

$$R_{\mathrm{r}} \quad \left(\frac{1}{R_1} + \frac{1}{R_2}\right)^{-1}. \tag{31}$$

According to Popov et al. (2019), the resulting normal contact force of a contact between a rigid cylinder with radius R and an elastic half space is given by

$$F_n = 2RE^{*}d. \tag{32}$$

For the following tests, we consider a contact of two materials with $E_A = 0.01$ GPa, $\nu_A = 0.5$ as well as $E_B = 200$ GPa and $\nu_B = 0.3$. Additionally, we resolve the smallest diameter with eight cells for the contact detection and use $k = 4/(3\sqrt{\pi})$ for all except the cylindrical flat punch case, where we use $k = 2/\sqrt{\pi}$.

4.1.2. Results

Fig. 3 shows the comparison of the analytical solutions as a solid line and computational results with different contact resolutions N_c. It is evident that for smaller resolutions, the resulting force has large deviations. Sometimes, the contact force is even mistakenly assumed to be 0. However, the results improve with increasing resolution, as expected. For a resolution of $N_c = 8$, this already leads to a good agreement of the simulation results with the analytical solutions, and larger resolutions provide an even better accuracy.

4.1.3. Grid independence

To confirm the grid independence, we calculate the root mean square relative error from the numerical results and analytical solutions provided in Section 4.1.2. Previously, we considered different radii. In Fig. 4, however, the average errors of the respective test cases are plotted over the dimension of the overlap N_c and the indentation depth $d = 0$ remains unconsidered. In addition, we compare the data with the experimental order of convergence, EOC = 1 and EOC = 2. As expected, a reduction of the error with increasing resolution is noticeable. Furthermore, we see in large parts of the diagram that a linear slope similar to the EOC = 1 exists, i.e., doubling the resolution halves the error. However, outliers occur because the anisotropic voxel representation in some cases over and in other cases underestimates curved surfaces.

4.2. Cylinder wall impact

As a further test, the impact of a cylinder on a plane wall is investigated. Since results for this are known from the literature (Park, 2003), this case is frequently considered (Kodam et al., 2010; Rakotonirina et al., 2019).

Fig. 5 shows the basic setup. A cylinder with radius R and height H moves at a constant velocity v_z^- toward the wall located on the x axis since no fluid is present. Furthermore, there is no friction between the cylinder and the wall.

According to Park (2003), the post impact angular velocity reads

$$\omega_y^+ = \frac{m v_z^-(1+e) r\cos(\alpha+\theta)}{I_{yy} + m r^2 \cos^2(\alpha+\theta)}, \tag{33}$$

with the mass of the cylinder m, the signed coefficient of restitution $e = v_z^+/v_z^-$ that depends on the post impact velocity v_z^+, the moment of inertia with respect to the y axis I_{yy}, and the distance between the impact point $\boldsymbol{C}$ and the center of the cylinder $r = \sqrt{R^2 + \frac{1}{4}H^2}$. Additionally, two angles influence the outcome. One is the impact angle θ, which can take values between 0° and 90°and the other one is α, which is the angle between the line from the point of impact to the center of the cylinder and the face of the cylinder. There is also a solution for the rebound velocity (Park, 2003)

$$v_z^+ = \omega_y^+ r\cos(\alpha+\theta) - e v_z^-. \tag{34}$$

In the following, we consider a cylinder with a height $H = 0.0053$ m, radius $R = 0.004$ m, mass $m = 3.1 \cdot 10^{-4}$ kg and a moment of inertia $I_{yy} = I_{xx} = 1.96566 \cdot 10^{-9}$ kg m^2 and $I_{zz} = 2.48 \cdot 10^{-9}$ kg m^2. Furthermore, the cylinder settles with an initial velocity of $v_z^- = 1$ m/s. The cylinder's radius is resolved by a resolution of $N = 4$, for the on lattice contact detection. However, for the rest of the contact treatment, the resolution N_c varies as is visible in Fig. 6(a)–(b). Additionally, we use time steps of $\Delta t \approx 1.7 \cdot 10^{-6}$ s. When a collision is detected, we reduce the time step size and use $\Delta t_c = \Delta t/10$ instead. Furthermore, we set $c = 0.264$ s/m since this corresponds to a coefficient of restitution of about 0.85, thus $e = 0.85$ applies. The modulus of elasticity is $E = 5 \cdot 10^8$ Pa for both the wall and particle. Following Kodam et al. (2010), we set the Poisson's ratio ν both times to 0.35.

In Fig. 6(a), we compare the resulting de dimensionalized rebound velocity from our simulations with the analytical solution mentioned before Eq. (34) and simulations by Kodam et al. (2010) using three layers of glued spheres and Rakotonirina et al. (2019) using three glued cylinders. Furthermore, we plot the de dimensionalized angular velocities versus the analytical solution Eq. (33) and numerical results in Fig. 6(b). In both figures, we consider post collision values.

We see in both cases that a low resolution, $N_c = 2$, again yield less satisfactory results. However, a good agreement with the comparison data is already obvious from a resolution of $N_c = 4$, which becomes even better with further increasing resolution. It is visible that the simulation data conform to the solid line of the analytical solution. This agreement is better than for the three layers of glued spheres by Kodam et al. (2010) illustrated as blue crosses and similar to consideration of three glued cylinders by Rakotonirina et al. (2019) illustrated as orange crosses. For the latter, good results are expected, since a cylinder can be perfectly composed of smaller cylinders. For more complex geometries, however, a perfect match may not be possible and the results may decrease in accuracy similar to the glued spheres. In general, this test case shows a very good accuracy of the proposed novel method.

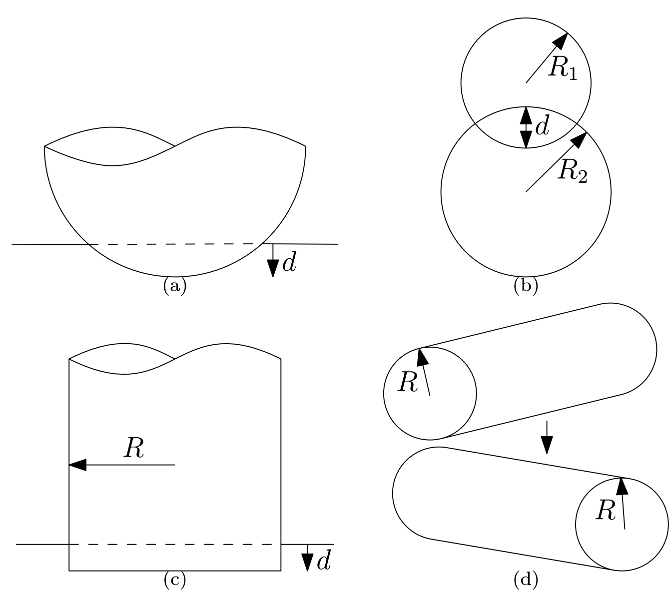

Fig. 2. Sketches of the considered test cases with an indentation depth d: (a) contact between a sphere with radius R and a half-space, (b) contact between two spheres with radii R_1 and R_2, (c) contact between a cylinder with radius R and a half space, and (d) contact between two perpendicular crossed cylinders with the same radius R.

5. Particle rebound in viscous fluid

In the following chapter, we deal with a collision between a spherical particle and a resting wall in a viscous fluid to further validate the presented method and to show its potential.

5.1. Description

We numerically study the experimental setup by Li (2010) in which spherical particles with a radius of 4.75 mm, a density of 7780 kg/m^3 and a moment of inertia of 3.15207 $\cdot$ 10^{-8} kg m^2 are released from different heights. We consider the initial heights h_0 of 5.5 mm, 19.6 mm and 35.7 mm to cover the range of experiments. The surrounding fluid is an aqueous glycerol solution that has a density and viscosity of 1230 kg/m^3 and 50.2 $\cdot$ 10^3 Pa$\cdot$s, respectively.

In the numerical setup, we consider a closed container with a height of 0.05 m and an equally sized length as well as width of 0.042 m. For the walls, we use a no slip halfway bounce back condition (Sukop & Thorne, 2006). Furthermore, we set the

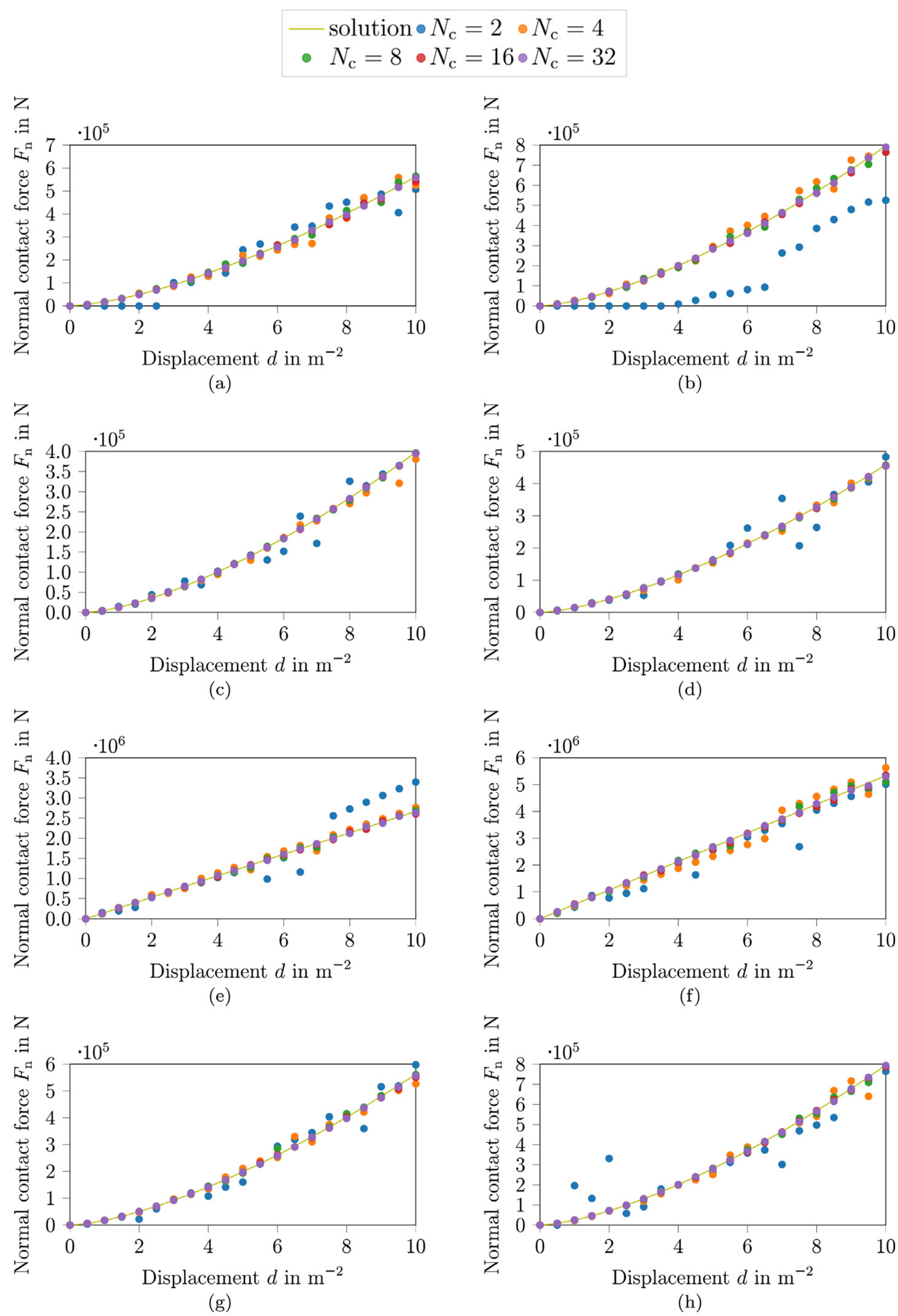

Fig. 3. Comparison of the analytical solution for the normal contact force F_n over the indentation depth d as a solid line with computational results for contact between (a) a sphere with radius R 1 m and a half-space, (b) a sphere with radius R 2 m and a half-space, (c) two spheres with equal radius R 1 m, (d) two spheres with radii R_1 1 m and R_2 2 m, (e) a cylinder with radius R 1 m and a half-space, (f) a cylinder with radius R 2 m and a half-space, (g) two crossed cylinders with equal radius R 1 m, and (h) two crossed cylinders with equal radius R 2 m.

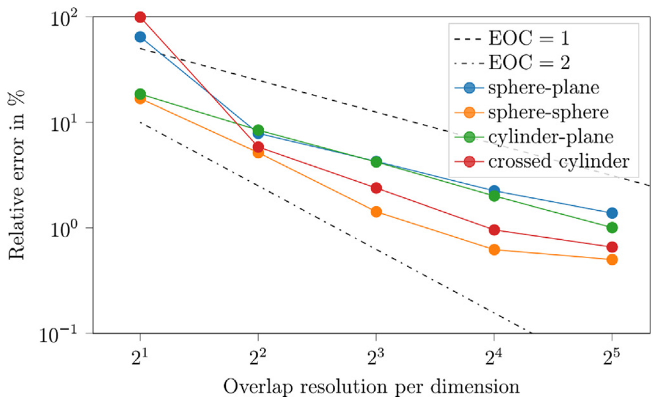

Fig. 4. Relative error versus overlap resolution per dimension N_c.

elasticity modulus of the particle to 20 GPa and of the wall to 3 GPa and use the damping constant c 0.12. Additionally, the Poisson's ratios of the particle and wall are 0.33 and 0.24.

We discretize the spatial domain by Δx 0.3 mm, and Δt 5 µs is the size of the time steps to solve the fluid with HLBM. To solve the equations of motion and calculate the contact force, we use smaller time steps of $\Delta t/1000$. For this, it is necessary to sufficiently resolve the time the particle and the wall are in contact. Also, we use an overlap resolution N_c 16. To avoid tiny channels between the particle and the wall and thus insufficiently studied nano effects, we enlarge the particle by $\Delta x/7$ solely for the collision consideration.

In this case, the tangential force is negligible. It therefore requires another benchmark with surrounding fluid for validation of the existing model in future considerations.

5.2. Results

A comparison of the results obtained by using the proposed novel method with the experimental results by Li (2010) and numerical results by Qiu and Wu (2014) is given in Fig. 7. In this figure, we see the minimum distance h from the falling sphere's surface to the bottom wall plotted over time. We consider three cases, as

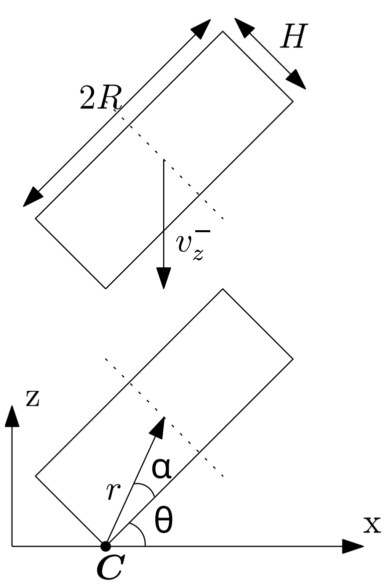

Fig. 5. Sketch of the normal cylinder-wall impact test case.

mentioned before. Different colors highlight these. Thereby, the simulation data are shown as dashed lines and the measurement data by Li (2010) as points and the results of Qiu and Wu (2014) as crosses.

In all cases, the ball first accelerates from its rest position h_0 towards the bottom wall. Due to varying drop heights, acceleration phases of different lengths are also noticeable. The subsequent contact with the wall causes the spherical particle to move upwards. Therefore, the distance h increases again. However, the height reached after the rebound is smaller than the initial height h_0 before and particles with greater drop height also rebound more strongly and reach a greater heights after the impact. This process is repeated until the ball comes to rest on the ground, as each time, it loses energy.

Overall, a good agreement of our results with the data by Li (2010) and Qiu and Wu (2014) is visible. Small deviations are particularly noticeable in the first impact from the highest falling height h_0, since the influence of the fluid is greatest there. We can see, for example, that in the same case, at the second impact, the

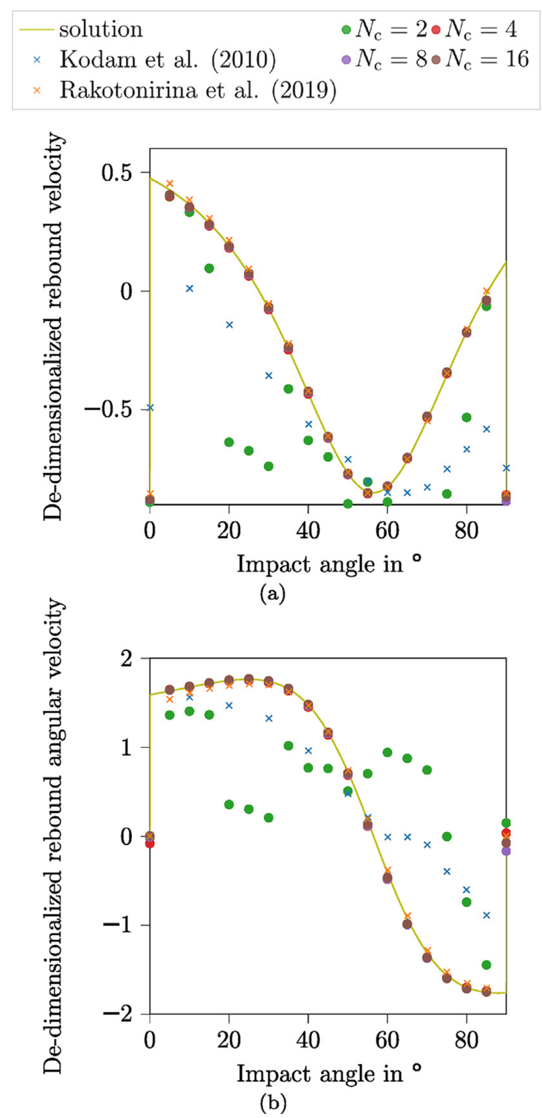

Fig. 6. Comparison of the analytical solution and computational results of dimensionless post-impact velocities for the collision of a cylinder and a wall. The plots show (a) the rebound velocity v_z^+/v_z and (b) the rebound angular velocity $r\omega_y^+/v_z$ over the impact angle θ.

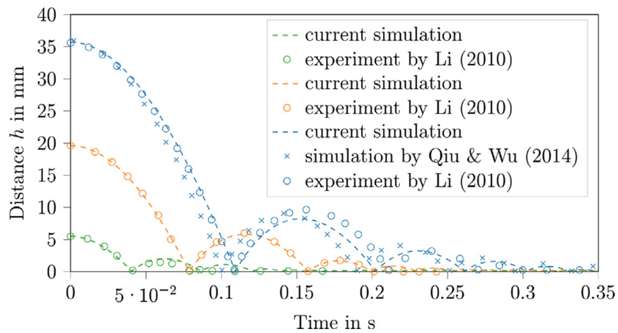

Fig. 7. Plot of the shortest distance between a settling sphere's surface and the bottom wall over time.

maximum rebound height corresponds to the measured values. Furthermore, deviations between the numerical results of the current simulation and the one of Qiu and Wu (2014) are evident in the initial acceleration of the sphere.

5.3. Discussion

We have shown that the proposed discrete collision model is capable of an accurate contact treatment for arbitrarily shaped particles. The contact model is essential in the considered case because without it there would be no rebound and only a decel eration of the particle. This reveals the great potential of this novel model for further studies of particulate flows of all kinds.

However, we also see that the method still has further potential for improvement. For example, the different heights after the first rebound of the sphere with an initial height of 35.7 mm in Fig. 7 are probably due to the assumption of a constant damping factor. Contrary to the assumption, the literature suggests that the damping depends on the initial relative velocity of the two objects in contact.

The differences between the current and the results by Qiu & Wu (2014) in the initial particle acceleration are because of the surface resolved particles in this work and the resulting advantages in the determination of hydrodynamic forces.

It is also evident that it is important to study the mechanics of almost collisions, especially for viscous fluids. This is due to the fact that the formation of nanoscale channels may induce other effects. As we have shown, it is possible to model the collision by a virtual particle enlargement. However, further studies are required to find an optimal parameter which influences the accuracy of the result solely positively.

6. Summary and conclusions

In this paper, we propose a novel contact model for complex arbitrary shaped convex geometries and show that it describes contacts with high accuracy. This is highlighted multiple times in various cases, where we verify the correctness of the contact force and the resulting motion of a particle with and without a fluid present.

In the latter case, we furthermore demonstrate that the pro posed method works well with HLBM. However, other PSMs make no difference. With this contact model, it is now possible to simulate complex suspensions precisely and thus to study real world applications, e.g., hindered settling, extensively.

However, there is also potential for improvement, e.g. we recommend deriving the contact model parameter k directly from the respective shape of the overlap, which further improves the accuracy of the resulting force. Furthermore, future studies of the relationship between the damping factor c and the initial relative velocity have the potential to lead to improvements in the pro posed method. In addition, it is significant to model the respective fluid correctly, even with nano sized channels shortly before the collision. Alternatively, this is solvable by a virtual enlargement of the colliding objects. However, this solution also requires further investigations. Additional studies are also desired for validation of the tangential force in the presence of a (viscous) fluid.

Overall, the novel method suits the previously mentioned challenges well and can be used flexibly with different methods for particulate flows, such as PSMs.

Declaration of competing interest

The authors declare that they have no known competing financial interests or personal relationships that could have appeared to influence the work reported in this paper.

Acknowledgements

The research leading to these results was conducted during the IGF Project AiF 21096 N of the FEI that has been supported via AiF within the programme for promoting the Industrial Collective Research (IGF) of the Federal Ministry of Economic Affairs and Climate Action (BMWK) based on a resolution of the German Parliament.

References

Alves, J., Peixinho, N., da Silva, M. T., Flores, P., & Lankarani, H. M. (2015). A comparative study of the viscoelastic constitutive models for frictionless contact interfaces in solids. *Mechanism and Machine Theory*, *85*, 172 188. https://doi.org/10.1016/j.mechmachtheory.2014.11.020

Bhatnagar, P. L., Gross, E. P., & Krook, M. (1954). A model for collision processes in gases. i. small amplitude processes in charged and neutral one-component systems. *Physical Review*, *94*(3), 511 525. https://doi.org/10.1103/PhysRev.94.511

Carvalho, A. S., & Martins, J. M. (2019). Exact restitution and generalizations for the hunt crossley contact model. *Mechanism and Machine Theory*, *139*, 174 194. https://doi.org/10.1016/j.mechmachtheory.2019.03.028

Džiugys, A., & Peters, B. (2001). An approach to simulate the motion of spherical and non-spherical fuel particles in combustion chambers. *Granular Matter*, *3*(4), 231 266.

Hart, J. C. (1996). Sphere tracing: A geometric method for the antialiased ray tracing of implicit surfaces. *The Visual Computer*, *12*(10), 527 545. https://doi.org/10.1007/s003710050084

Haugo, S., Stahl, A., & Brekke, E. (2017). Continuous signed distance functions for 3d vision. In *2017 international conference on 3D vision (3DV)* (pp. 116 125). https://doi.org/10.1109/3DV.2017.00023

Haussmann, M., Hafen, N., Raichle, F., Trunk, R., Nirschl, H., & Krause, M. J. (2020). Galilean invariance study on different lattice Boltzmann fluid solid interface approaches for vortex-induced vibrations. *Computers & Mathematics with Applications*, *80*(5), 671 691. https://doi.org/10.1016/j.camwa.2020.04.022

Kodam, M., Bharadwaj, R., Curtis, J., Hancock, B., & Wassgren, C. (2010). Cylindrical object contact detection for use in discrete element method simulations, part ii experimental validation. *Chemical Engineering Science*, *65*(22), 5863 5871. https://doi.org/10.1016/j.ces.2010.08.007

Krause, M. J., Avis, S., Kusumaatmaja, H., Dapelo, D., Gaedtke, M., Hafen, N., Haußmann, M., Jeppener-Haltenhoff, J., Kronberg, L., Kummerlander, A., Marquardt, J. E., Pertzel, T., Simonis, S., Trunk, R., Wu, M., & Zarth, A. (2020a). *OpenLB release 1.4: Open source lattice Boltzmann code*. Nov. https://doi.org/10.5281/zenodo.4279263.

Krause, M. J., Klemens, F., Henn, T., Trunk, R., & Nirschl, H. (2017). Particle flow simulations with homogenised lattice Boltzmann methods. *Particuology*, *34*, 1 13. https://doi.org/10.1016/j.partic.2016.11.001

Krause, M. J., Kummerlander, A., Avis, S. J., Kusumaatmaja, H., Dapelo, D., Klemens, F., Gaedtke, M., Hafen, N., Mink, A., Trunk, R., Marquardt, J. E., Maier, M.-L., Haussmann, M., & Simonis, S. (2020b). Openlb open source lattice Boltzmann code. *Computers & Mathematics with Applications*. https://doi.org/10.1016/j.camwa.2020.04.033

Krüger, T., Kusumaatmaja, H., Kuzmin, A., Shardt, O., Silva, G., & Viggen, E. M. (2017). *The lattice Boltzmann method, graduate texts in physics*. Springer. https://doi.org/10.1007/978-3-319-44649-3

Kupershtokh, A., Medvedev, D., & Karpov, D. (2009). On equations of state in a lattice Boltzmann method. *Computers & Mathematics with Applications*, *58*, 965 974. https://doi.org/10.1016/j.camwa.2009.02.024

Li, X. (2010). *An experimental and numerical study of normal particle collisions in a viscous liquid*. Ph.D. thesis. California Institute of Technology. https://doi.org/10.7907/S5V0-3E25.

Nagata, T., Hosaka, M., Takahashi, S., Shimizu, K., Fukuda, K., & Obayashi, S. (2020). A simple collision algorithm for arbitrarily shaped objects in particle-resolved flow simulation using an immersed boundary method. *International Journal for Numerical Methods in Fluids, 92*(10), 1256 1273. https://doi.org/10.1002/fld.4826

Nassauer, B., & Kuna, M. (2013). Contact forces of polyhedral particles in discrete element method. *Granular Matter, 15*(3), 349 355. https://doi.org/10.1007/s10035-013-0417-9

Noble, D. R., & Torczynski, J. R. (1998). A lattice-Boltzmann method for partially saturated computational cells. *International Journal of Modern Physics C, 9*(8), 1189 1201. https://doi.org/10.1142/S0129183198001084

Nolan, G. T., & Kavanagh, P. E. (1995). Random packing of nonspherical particles. *Powder Technology, 84*(3), 199 205. https://doi.org/10.1016/0032-5910(95)98237-S

Park, J. (2003). *Modeling the dynamics of fabric in a rotating horizontal drum*. Ph.D. thesis. Purdue University.

Popov, V. L. (2017). *Contact mechanics and friction: Physical principles and applications* (2nd ed.). Springer Nature. https://doi.org/10.1007/978-3-662-53081-8

Popov, V. L., Heß, M., & Willert, E. (2019). *Handbook of contact mechanics: Exact solutions of axisymmetric contact problems*. Springer Nature. https://doi.org/10.1007/978-3-662-58709-6

Qiu, L.-c., & Wu, C.-y. (2014). A hybrid dem/cfd approach for solid-liquid flows. *Journal of Hydrodynamics, 26*, 19 25. https://doi.org/10.1016/S1001-6058(14)60003-2

Rakotonirina, A. D., Delenne, J.-Y., Radjai, F., & Wachs, A. (2019). Grains3d, a flexible dem approach for particles of arbitrary convex shape part iii: Extension to non-convex particles modelled as glued convex particles. *Computational Particle Mechanics, 6*(1), 55 84. https://doi.org/10.1007/s40571-018-0198-3

Rakotonirina, A. D., & Wachs, A. (2018). Grains3d, a flexible dem approach for particles of arbitrary convex shape - part ii: Parallel implementation and scalable performance. *Powder Technology, 324*, 18 35. https://doi.org/10.1016/j.powtec.2017.10.033

Succi, S. (2001). *The lattice Boltzmann equation: For fluid dynamics and beyond*. Oxford university press.

Sukop, M. C., & Thorne, D. T. (2006). *Lattice Boltzmann modeling: An introduction for geoscientists and engineers* (2nd ed.). Springer. https://doi.org/10.1007/978-3-540-27982-2

Sun, R., & Xiao, H. (2016). Sedifoam: A general-purpose, open-source cfd dem solver for particle-laden flow with emphasis on sediment transport. *Computers & Geosciences, 89*, 207 219. https://doi.org/10.1016/j.cageo.2016.01.011

Swope, W. C., Andersen, H. C., Berens, P. H., & Wilson, K. R. (1982). A computer simulation method for the calculation of equilibrium constants for the formation of physical clusters of molecules: Application to small water clusters. *The Journal of Chemical Physics, 76*(1), 637 649. https://doi.org/10.1063/1.442716

Trunk, R., Bretl, C., Thater, G., Nirschl, H., Dorn, M., & Krause, M. J. (2021b). A study on shape-dependent settling of single particles with equal volume using surface resolved simulations. *Computation, 9*(44), 40. https://doi.org/10.3390/computation9040040

Trunk, R., Marquardt, J., Thater, G., Nirschl, H., & Krause, M. J. (2018). Towards the simulation of arbitrarily shaped 3d particles using a homogenised lattice Boltzmann method. *Computers & Fluids, 172*, 621 631. https://doi.org/10.1016/j.compfluid.2018.02.027

Trunk, R., Weckerle, T., Hafen, N., Thater, G., Nirschl, H., & Krause, M. J. (2021a). Revisiting the homogenized lattice Boltzmann method with applications on particulate flows. *Computation, 9*(22), 11. https://doi.org/10.3390/computation9020011

Uhlmann, M. (2005). An immersed boundary method with direct forcing for the simulation of particulate flows. *Journal of Computational Physics, 209*(2), 448 476. https://doi.org/10.1016/j.jcp.2005.03.017

Verlet, L. (1967). Computer "experiments" on classical fluids. I. Thermodynamical properties of Lennard-Jones molecules. *Physical Review, 159*(1), 98 103. https://doi.org/10.1103/PhysRev.159.98

Wachs, A., Girolami, L., Vinay, G., & Ferrer, G. (2012). Grains3d, a flexible dem approach for particles of arbitrary convex shape part i: Numerical model and validations. *Powder Technology, 224*, 374 389. https://doi.org/10.1016/j.powtec.2012.03.023

Weers, M., Hansen, L., Schulz, D., Benker, B., Wollmann, A., Kykal, C., Kruggel-Emden, H., & Weber, A. P. (2022). Development of a model for the separation characteristics of a deflector wheel classifier including particle collision and rebound behavior. *Minerals, 12*(4), 480. https://doi.org/10.3390/min12040480

Wen, B., Zhang, C., Tu, Y., Wang, C., & Fang, H. (2014). Galilean invariant fluid solid interfacial dynamics in lattice Boltzmann simulations. *Journal of Computational Physics, 266*, 161 170. https://doi.org/10.1016/j.jcp.2014.02.018

Zhu, H. P., Zhou, Z. Y., Yang, R. Y., & Yu, A. B. (2008). Discrete particle simulation of particulate systems: A review of major applications and findings. *Chemical Engineering Science, 63*(23), 5728 5770. https://doi.org/10.1016/j.ces.2008.08.006